Engineering Fracture Mechanics 168 (2016) 26–45

Contents lists available at ScienceDirect

Engineering Fracture Mechanics

journal homepage: www.elsevier.com/locate/engfracmech

Numerical simulation of ductile crack growth in medium wide plate specimens using 3-D computational cells

Diego F.B. Sarzosa [a,*], Matthias Verstraete [b], Stijn Hertelé [b], Rudi Denys [b], Claudio Ruggieri [a]

[a] Department of Naval Architecture and Ocean Engineering, University of São Paulo, São Paulo, Brazil
[b] Department of Mechanical Construction and Production, Ghent University, Gent, Belgium

ARTICLE INFO

Article history:
Received 15 April 2016
Received in revised form 5 September 2016
Accepted 16 September 2016
Available online 20 September 2016

Keywords:
Curved Wide Plate
Constraint
Ductile tearing
Gurson-Tvergaard damage model
Cell methodology

ABSTRACT

This work examines the applicability of a local damage method based on the computational cell methodology, incorporating the Gurson-Tvergaard (GT) yielding model, to predict ductile crack extension of circumferential crack-like defects in Medium Wide Plates (MWP) specimens, extracted from girth welds of pipelines, using standard single edge bend SE(B) specimen and recently standardized clamped single edge tension SE(T) specimens to obtain model parameters. Laboratory testing of SE(B) and SE(T) specimens at room temperature provides necessary and sufficient information to calibrate the parameters of the GT yielding law. After the model parameters have been defined using small specimens, predictions of crack growth behavior can be carried out for other geometries and loading modes. Therefore, parameter transferability between different specimens can be investigated and comparative studies of predicted crack driving forces can be performed. In this study, the simulated tearing resistance curves are compared to experimental data of MWP specimens, where the former is obtained by the cell model calibrated using either SE(T) or SE(B) specimens and the latter is obtained by large-scale experiments. Overall, a good agreement between numerical and experimental $\delta - \Delta a$ curves was observed demonstrating that the cell methodology can be considered as a valid engineering tool for studying the integrity of structural components.

1. Introduction

The efficient and safe use of the fracture mechanics approach to the design of new structural components and repair decisions of typical in-service flaws assumes that fracture toughness values measured from testing standard specimens are a material property. Within this methodology, experimentally measured fracture toughness values can be *transferred* in a rather straightforward manner to structural applications provided the crack-tip conditions between the laboratory specimen and the structure are presumably similar (see, *e.g.* - Hutchinson [1] and Anderson [2]). However, while single-parameter fracture mechanics approaches provide a generally conservative acceptance criterion for cracked structural components by relating the operating conditions to a critical applied load or critical crack size, these approaches are not appropriated to describe adequately the crack-tip stresses and strains which drive the fracture process when large-scale plasticity develops in the specimen or structure. A particular case of considerable interest lies in direct application of crack growth resistance ($J - \Delta a$ or $\delta - \Delta a$) curves (also often termed R-curves) measured using small laboratory specimens to surface defects in larger

* Corresponding author.
E-mail address: dsarzosa@gmail.com (D.F.B. Sarzosa).

http://dx.doi.org/10.1016/j.engfracmech.2016.09.008
0013-7944/

Nomenclature

σ_e	effective von Mises stress
σ_m	mean hydrostatic stress
$\bar{\sigma}$	current flow stress of the cell matrix material
f	initial void volume divided by cell volume
q_i $(i = 1, 2, 3)$	dimensionless factors to improve cell response
f_E	critical void value
D	cell size
a	crack depth
c	crack length
n	strain hardening exponent
K	strength coefficient
Δa	amount of stable crack growth
H	length of SE(T) specimen
S	unsupported span of the SE(B) specimen
D'	external pipe diameter
t	pipe wall thickness
W'	width of the Medium Wide Plate specimen
L	length of the prismatic section of Medium Wide Plate specimen
$2h$	weld groove width
B	specimen thickness
B_N	net specimen thickness
δ	crack tip opening displacement (CTOD)
J	J-integral
a/W	crack size ratio
σ_{ys}	tensile yield strength
σ_{uts}	ultimate tensile strength

structural components. However, laboratory testing of fracture specimens to measure resistance curves consistently reveals a marked effect of absolute specimen size, geometry, relative crack size (a/W) and loading mode (tension vs. bending) on R-curves. These effects arise from the strong interaction between micro-structural features of the material, which govern the actual separation process, and the loss of stress triaxiality in the crack front region due to large-scale yielding.

The latter is often referred to as crack-tip constraint. This constraint, for either a structural component or a test specimen, can be interpreted as the ability to deform plastically under increasing levels of remote applied load. Current engineering approaches for defect assessments make extensive use of fracture toughness values measured from testing high constraint fracture specimens, such as deeply-cracked C(T) or SE(B) geometries, to characterize the material fracture behavior at a specific temperature. However, structural components, that have been just manufactured or have been operating under normal conditions, usually contain shallow cracks which are associated with low levels of constraint. Thus, direct application of fracture toughness data from high constraint specimens to low constraint structures often introduces high levels of conservatism during the engineering analysis which are associated with unknown levels of safety. Consequently, advanced methodologies for structural integrity assessments endeavor to utilize fracture toughness data obtained from low constraint fracture specimens to provide more adequate safety levels in design and in-service operation producing less conservative, but yet reliable, engineering structures.

Within this context, recent fracture assessment guidelines recommended by Det Norske Veritas [3] and British Standard [4] advocate the use of single edge notch tension (SE(T)) specimen under clamped conditions to characterize the fracture properties of high pressure piping systems. The primary advantage to use SE(T) specimen to describe the fracture toughness curve is the similarity in the crack tip fields (stresses and strains) between the SE(T) geometry and pipeline girth welds under global bending. Another advantage of this specimen is that the actual crack depth in the SE(T) specimen is not essential for obtaining a representative $\delta(J) - \Delta a$ curve, as long as it is between $0.3 \leqslant a/W \leqslant 0.5$ [5]. This feature has also been observed by previous numerical simulations [6]. Recent applications of SE(T) specimens to characterize crack growth resistance properties in a high strength API 5L X100 steel [7] have been effective in providing large flaw tolerances and reducing the excessive conservatism obtained with testing of high constraint specimens.

Another geometry that deserves attention is the Curved Wide Plate (CWP) specimen. The CWP was introduced by researchers of University of Ghent in Belgium in the 1970s [8]. The CWP specimen takes into account different factors such as crack-tip constraint, component scale volume sampling, and heterogeneous mechanical properties in welded joints affecting the response of real welded structures - including - pipelines, pressure vessels, and naval applications. These structures are typically subjected to membrane tension loads, that is, small stress variation through the thickness direction. In the case of pipelines, a curved wide plate (CWP) is extracted from the girth welds and has the advantage of behaving (in mechanical

sense) in a similar way to the pipeline [8–11]. This may involve the introduction of a correction factor to account for the effect of internal pressure on tensile strain capacity obtained by CWP specimens. Chen and Lambert [12] have carried out numerical studies of wide plates using a damage model. They reported discrepancies between the predictions and experiments of load versus CMOD curve less than 10%. Recent work of Hertelé et al. [13] introduced a smaller curved wide plate, named medium wide plate (MWP), as a research oriented alternative to improve the understanding of fracture behavior of curved plates by means of advanced instrumentation, such as the digital image correlation technique. The major benefit of testing MWP specimen is the reduced investment, in terms of time and funding, as compared to full-scale tests of real structures or CWP tests.

Motivated by these observations, this investigation explores the ability of a micromechanics approach, based upon the computational cell methodology incorporating the Gurson-Tvergaard (GT) yielding model, to describe ductile crack response of notched curved wide plates subjected to large deformation levels. The central focus of this article is to describe ductile fracture behavior for the recently developed Medium (Curved) Wide Plate specimen. The numerical analyses are supported by results that have been obtained using the experimental facilities at the Soete Laboratory of University of Ghent by Verstraete [14,15]. A computational cell methodology to model Mode I crack extension in ductile materials is utilized to describe the evolution of CTOD with the accompanying evolving near-tip stress-strain fields. Experimental crack growth resistance curves from a high constraint specimen, SE(B), and a low constraint specimen, SE(T), are used to calibrate the constitutive material model proposed by Gurson [16] and Tvergaard [17]. The calibrated GT parameters are then used to predict the resistance curves. Finally, the numerically predicted and the experimentally measured resistance curves are directly compared for the MWP specimens.

2. Overview of the computational cell methodology for modeling ductile tearing

This section presents a brief overview of the cell-based framework to model stable crack growth in ductile materials. Further details of the cell model are found in [18–21].

Experimental observations and computational studies show that the plastic strain for nucleation of microvoids by fracture or decohesion of the largest inclusions is small, thereby causing only little damage in the material ahead of the crack tip [2,19,21–23]. This feature enables simplification of the ductile failure process by assuming the growth of microvoids as the critical event controlling ductile extension. Fig. 1(a) illustrates a simplified view of the conditions ahead of a macroscopic crack front in a ductile material. The material layer enveloping the growing crack identifies a process zone for the ductile fracture which provides the necessary length dimension for the model. Void growth and coalescence in the layer will cause the surface traction exerted by the process zone on its surroundings to reduce to zero. Using the previous statements, Xia and Shih [18] proposed a model using computational cells to include a realistic void growth mechanism and a microstructural length-scale physically coupled to the size of the fracture process zone. Void growth remains confined to a layer of material symmetrically located nearby the crack plane, as illustrated in Fig. 1(b), and having thickness D, which is associated with the mean spacing of the larger, void initiating inclusions. This layer consists of cubical cell elements with dimension $D/2$ on each side; each cell contains a cavity of initial volume fraction f_0 (the initial void volume divided by cell volume), which roughly represents the actual metallurgical features of the material. As a further simplification, the void nucleates from an inclusion of relative size f_0 immediately upon loading.

Progressive void growth and subsequent macroscopic material softening in each cell are described with the Gurson-Tvergaard (GT) constitutive model for dilatant plasticity [16,17]. Gurson [16] proposed a plastic flow criterion including the volume of voids f and the mean hydrostatic stress σ_m in the yielding function, $\Phi = f(J_2, \sigma_m, f)$, as principal parameters driving the loss of load-carrying capacity of a material point. The progressive growth of the voids and corresponding reduction in the load-carrying capacity of the material are described by the following yield surface:

$$\Phi(\sigma_e, \sigma_m, \bar{\sigma}, f) = \sigma_e - \omega(\sigma_m, \bar{\sigma}, f)\bar{\sigma} = 0 \tag{1}$$

$$\omega(\sigma_m, \bar{\sigma}, f) = \left[1 - 2q_1 f \cosh\left(\frac{3q_2\sigma_m}{2\bar{\sigma}}\right) + q_3 f^2\right]^{\frac{1}{2}} \tag{2}$$

where σ_e denotes the effective von Mises (macroscopic) stress, σ_m is the mean (macroscopic) stress, $\bar{\sigma}$ is the current flow stress of the cell matrix material and f defines the current void fraction. Factors q_1, q_2 and q_3 introduced by Tvergaard [17] improve the model predictions for periodic arrays of cylindrical and spherical voids.

When f in the cell incident on the current crack tip reaches a critical value, f_E, the computational procedures remove the cell thereby advancing the crack tip in discrete increments of the cell size (Tvergaard [17] refers to this process as the element extinction or vanish technique). The element extinction process defines the numerical procedure used to eliminate the cell from the finite element model after reaching the critical void size f_E. Specifically, the procedure specifies how the nodal forces are relaxed to zero and the reduction in element stiffness to zero. Ruggieri and Dodds [24,22] and Gullerud et al. [20] implemented a cell extinction process using a linear-traction separation model with a typically assigned value of f_E = 0.15–0.20. The final stage of void linkup with the macroscopic crack front then occurs by reducing the remaining stresses to zero in a prescribed linear manner. For further details of the numerical implementation the reader should review [18,20,22].

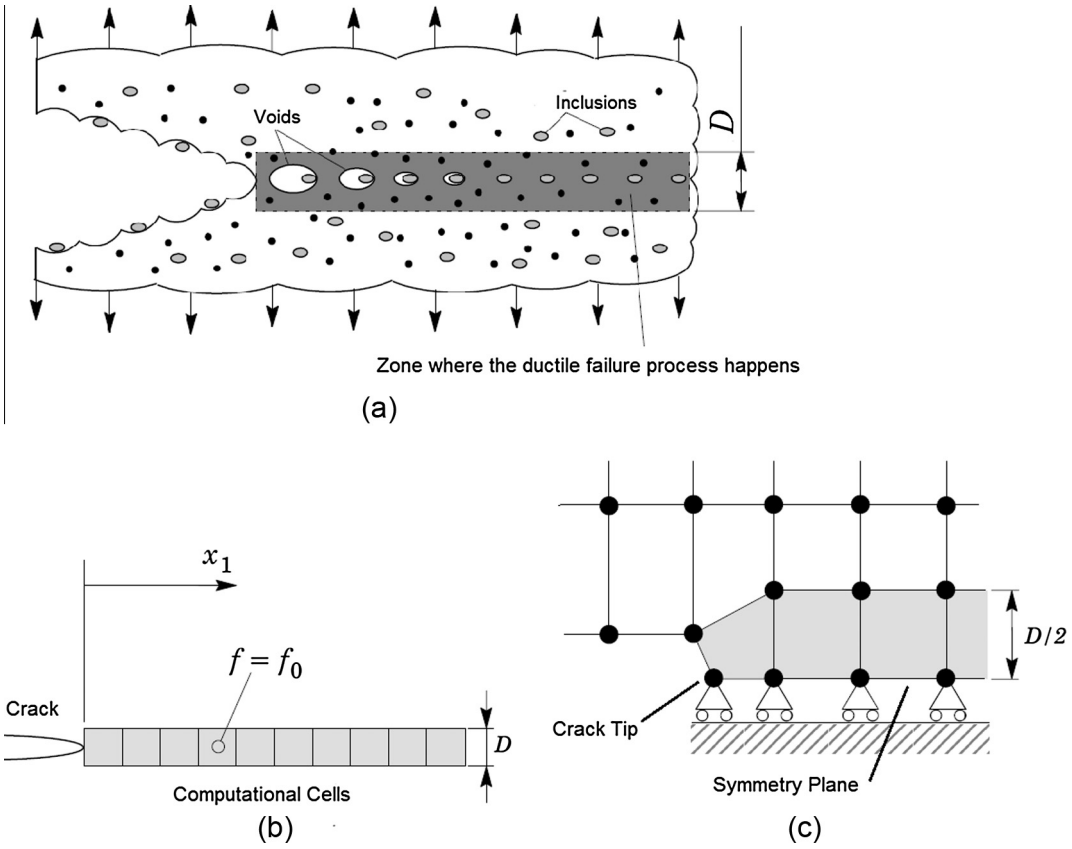

Fig. 1. Model for ductile crack growth using computational cells.

The plastic flow law proposed by Gurson-Tvergaard focuses on the description of growth of spherical voids under high levels of stress triaxiality. For low stress triaxiality, which is associated with areas of high plastic deformation, the actual decrease in load-bearing capacity of the material is not necessarily well described by Eq. (1) [25]. Consequently, an appropriate simulation of ductile fracture behavior may not be possible for geometries or structures with very low levels of stress triaxiality where the fracture failure is driven by shear fracture mechanism. Thus, the GT yielding model may be considered doubtful for low constraint conditions, and this study will investigate whether it is nevertheless possible to investigate its suitability under such conditions (e.g. SE(T) and MWP specimens).

3. Experimental testing

Verstraete et al. [15] studied the applicability and validity of SE(T) and Medium Curved Wide Plate (MWP) specimens to characterize fracture toughness properties and strain capacity in girth welded pipelines used for oil and gas transportation. This section provides a brief description of experimental tests performed in that study. The necessary data used as input for the numerical modeling are shown in this section. For more specific details about experimental measurement procedures the reader should review [14,15]. As previously described, Curved Wide Plate testing shows some advantages when compared to full-scale pipe testing. First, testing CWP is cheaper than testing full pipes. Second, there are a lot of previous data of CWP tests in the oil and gas industry that serve as database to create reliable guidelines for fracture assessment procedures for pipelines (e.g., the EPRG Tier 2 guidelines for the assessment of defects in transmission pipeline girth welds [26]). Third, it is possible to study and identify the variability of weld properties in girth welds related to the circumferential position of the weld and also the weld-to-weld process variations. Finally, CWP testing allows to adequately document the tested materials by extracting small-scale tensile and toughness specimens in the vicinity of the CWP specimen. The chosen materials for performing the numerical studies are the homogeneous base metal API 5L X65 steel and one girth weld made by welding an API 5L X80 base pipe with GMAW process.

Fig. 2 shows the geometry and specimen dimensions for the analyzed crack configurations: a Medium Wide Plate (MWP) specimen, a clamped single edge tension SE(T) specimen, and a 3-point bend SE(B) specimen. Here, L is the length of the prismatic section of MWP, D' is the external pipe diameter, W' is the width of the MWP specimen, t is the pipe wall thickness, a is the crack depth, and c is the crack length. As regards small-scale testing, H is the length of SE(T) specimen daylight between

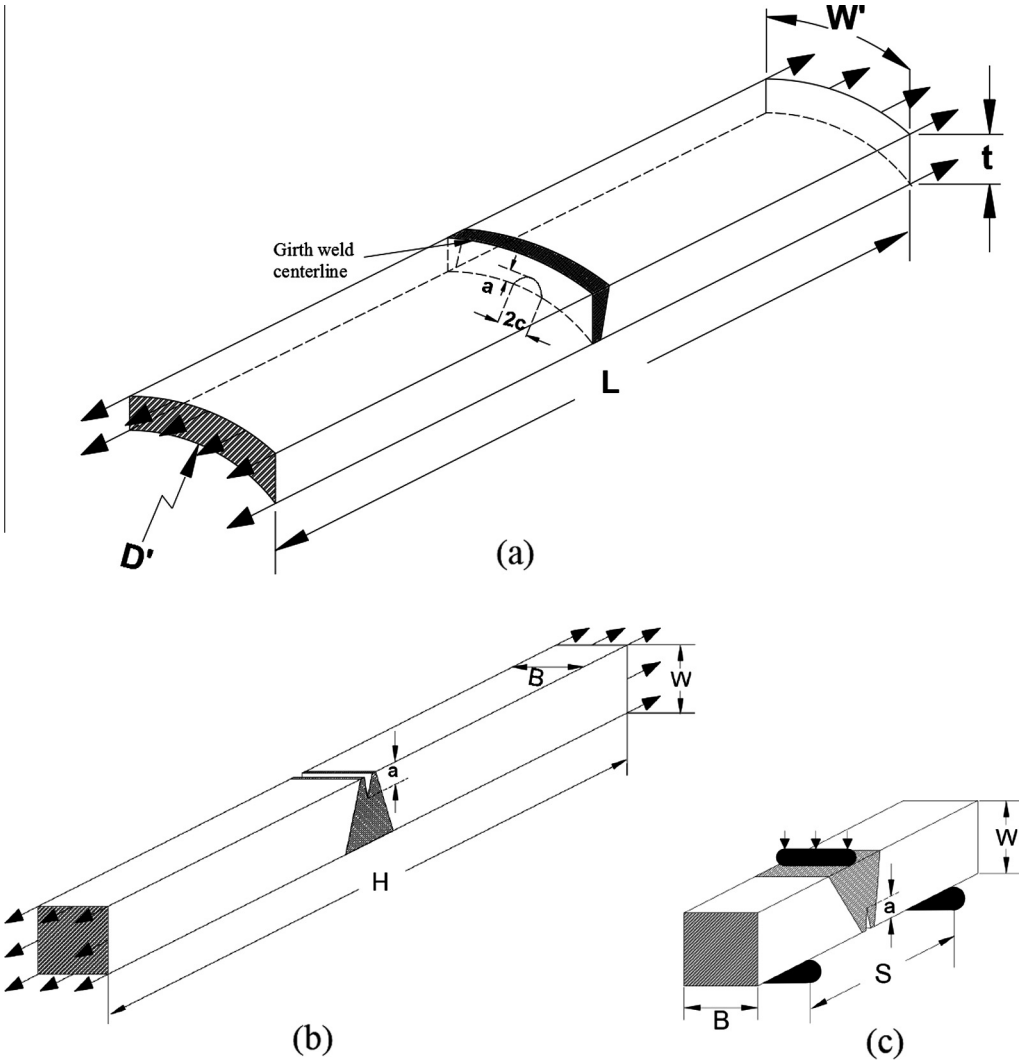

Fig. 2. Main dimensions of fracture specimens; (a) Medium Curved Wide Plate; (b) clamped SE(T) specimen; (c) 3 point bend SE(B) specimen.

grips, S is the unsupported span of the SE(B) specimen, a is the crack depth, and B is the specimen thickness. MWP specimens were flame cut from the pipes. The SE(B) and SE(T) configurations were extracted from the longitudinal direction of pipes for the girth welded pipe and from the rolling direction for the homogeneous flat plate. For the welded specimens, the notches were centered at the weld metal centerline and the defect was machined at the inner diameter surface (weld root side). The notch on the MWP specimen was milled using a 63 mm diameter saw blade, producing a notch tip radius of 75 μm. Fig. 3 is a picture of the girth weld joint tested by [14]. The relevant dimensions of each specimen are listed in Table 1.

Square cross-sectional SE(T) specimens were cut from the girth welded pipe. In order to take into account the intrinsic heterogeneous nature of the weld properties, the SE(T) specimens were sampled adjacent to the position where the MWP specimens were extracted. After extracting the specimens, they were notched through saw-cutting in two steps. The last step involved a fine saw blade having a tip radius of 75 μm. For sufficiently ductile materials, specimens with this initial notch will provide similar R-curves than fatigue precracked specimens [27,28]. Therefore, fatigue precracking was not applied. To improve crack front straightness, v-shaped side grooves were machined at both sides of the specimen. The side-groove depth was 7.5% on each side giving a net specimen thickness (B_N) equal to 0.85B. The side-grooves were machined according to the ASTM E1820 standard requirements [29], that is root radius in the range of 0.5 ± 0.2 mm and angle less than 90°. Regarding the homogeneous metal, identical procedure was followed to prepare the base metal SE(T) samples.

The SE(T) specimens were clamped using hydraulic grips mounted in a 150 kN tensile test rig and loaded in constant displacement rate mode (0.01 mm/s). The specimens are loaded beyond maximum force in the load-displacement curve. To obtain a sufficient amount of ductile crack extension, the tests were continued until the force drops back to 80% of the maximum recorded value.

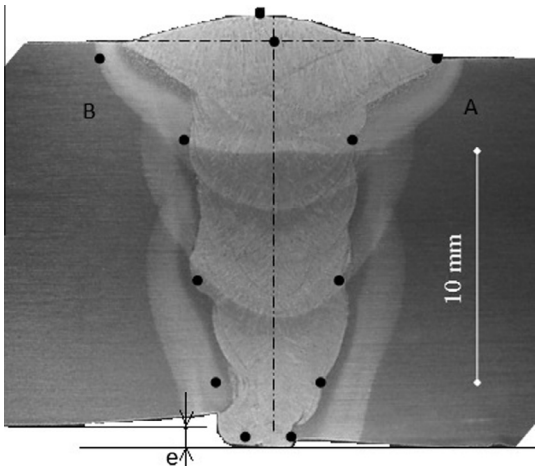

Fig. 3. Macrograph of the girth weld joint.

Table 1
Main physical dimensions for each sample.

Description	Homogeneous base metal	Girth welded pipe
SE(T) specimen		
W [mm]	14	14
a_0/W	0.2	0.3
W/B	1	1
H/W	10	10
SE(B) specimen		
W [mm]	14	14
a_0/W	0.5	0.5
W/B	1	1
S/W	4	4
MWP specimen		
W [mm]	150	150
t [mm]	15	17
a/t	0.20	0.30
c/a	10.0	4.75
D'/t	∞	71.7
L/W	3.30	3.30

Additionally, fracture toughness tests of deep crack side-groove bending specimens were conducted at room temperature for both materials. The notch was machined on the SE(B) specimen in identical procedure as made in the SE(T) specimen. To be consistent with the SE(T) test, fatigue precracking was not applied in this specimen. Side grooves were introduced to promote uniform crack growth ($B_N = 0.85B$) as well. The same experimental facilities used in testing the SE(T) specimen were employed to test the three point bend specimens. High constraint conditions were obtained by setting the crack size ratio equal to $\frac{a}{W} = 0.5$.

A tensile test rig with capacity of 2500 kN was used to test the MWP specimens. The test was stopped when the applied tensile force no longer exceeds 80% of its maximum. For both large-scale specimens, the introduction of notch at the specimen's central section is, similar to the SE(T) procedure, applied through saw-cutting with a similar, ultimately fine cutting blade. The specimen is loaded in tension with a constant displacement rate of 0.01 mm/s. The initial crack depths reflect those commonly considered in CWP testing. In contrast, the lengths are deliberately chosen relatively large to assure failure by means of unstable ductile crack extension rather than by plastic collapse [15].

3.1. Mechanical properties and measurement methods

3.1.1. The tensile stress-strain properties

The axial constitutive properties of the base pipeline metal were characterized by means of full thickness flat strip tensile test specimens. The weld metal was characterized using all weld metal round bar specimens extracted in the pipe's circumferential direction. Both types of tensile test specimens are in accordance with the standard EN 10002 [30]. Fig. 4 displays the measured engineering tensile stress-strain properties for the base metal pipeline API-5L X65 steel. The tensile yield strength

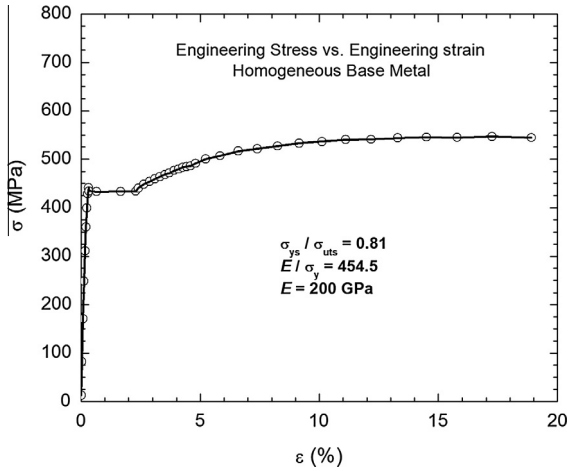

Fig. 4. Engineering tensile stress-strain properties for the API-5L X65 steel.

is σ_{ys} = 440 MPa and the ultimate tensile strength is σ_{uts} = 540 MPa. The true stress-strain curve after the Lüdder bands can be fitted to a power-law (i.e. $\sigma = K\epsilon^n$) relationship. For the base metal data the obtained strain hardening exponent and strength coefficient are $n = 0.186$ and $K = 386$ MPa, respectively. Other mechanical properties for the base material include Young's modulus E = 200 GPa and Poissons's ratio υ = 0.3.

Fig. 5 shows the tensile engineering stress-strain behavior response for the base metal pipeline steel (API 5L grade X80) and the corresponding weld metal. The yield strength of the weld metal is equal to σ_{ys} = 660 MPa and the ultimate tensile strength is σ_{uts} = 710 MPa. A power-law fit to the true stress-strain data, excluding the initial portion of the curve for which $\epsilon \leqslant 3\%$, yields the following coefficients: $n = 0.114$ and $K = 591$ MPa. In the same way, both strength characteristics are measured for the base metal pipe of API 5L grade X80 steel yielding the following values: σ_{ys} = 600 MPa and σ_{uts} = 675 MPa. The coefficients of a power-law curve representing the true stress-strain data are as follows: $n = 0.081$ and $K = 885$ MPa. The estimated Young Modulus is 205 GPa and 207 GPa for the base metal and weld metal, respectively. All tensile tests were performed at room temperature.

The measured tensile properties were used as input for the numerical analysis. The experimental engineering tensile curves were transformed into true (Cauchy) stress and logarithmic strain. The flow stress beyond necking is assumed to follow a power-law evolution.

3.1.2. Fracture toughness test procedure

Verstraete [14] determines the CTOD (δ) parameter using the double clip gauge methodology. The ductile crack growth, Δa, was estimated by two approaches: monitoring the elastic unloading compliance and measuring the direct current potential drop over the notch. For SE(T) specimens both methodologies of crack growth estimation provide similar results. On the

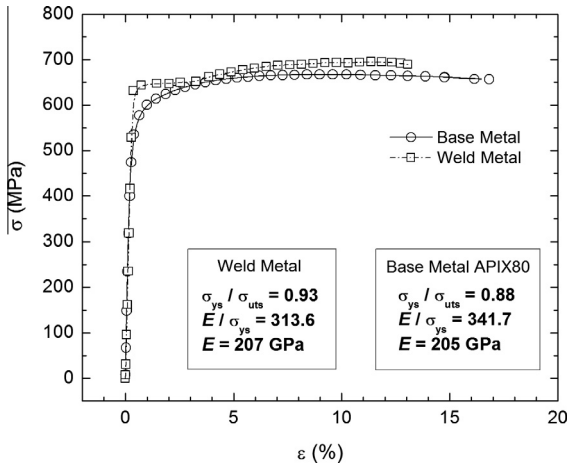

Fig. 5. Engineering tensile stress-strain curves for the API-5L X80 base metal and the weld metal.

other hand, physical crack growth measurements in MWP specimens are not straightforward and have been shown to be consistent only with the direct current potential drop methodology.

In all tests performed by Verstraete [14,15], in addition to remote force (P) and crack mouth displacement CMOD (Δ), two measurements of remote strain obtained by linear variable differential (LVDT) were reported. The CTOD is evaluated using the hinge model. This model assumes that the crack faces do not deform plastically and behave like two rigid parts which rotate around a single point. Using similar triangles between local and global measures of vertical crack flank displacement, CTOD (δ) can be estimated as [14]:

$$\delta = \left[\Delta_1 - (a_0 + z_1)\left(\frac{\Delta_2 - \Delta_1}{z_2 - z_1}\right)\right]\left(1 + \frac{\frac{\Delta_2 - \Delta_1}{2}}{z_2 - z_1}\right) \tag{3}$$

where Δ_1 and Δ_2 are displacement measures coming from two clip gages at two different heights ($z_1 = 2, z_2 = 8$) and a_0 is the initial crack size. It has to be noted that a correction factor has been included in Eq. (3). It was developed by Verstraete [14] to correlate the crack flank displacements measured using the 90° definition and the remote displacements above the crack mouth surface. In a similar way, the crack mouth opening displacement can be estimated by the following:

$$CMOD = \left(\frac{z_2\Delta_1 - z_1\Delta_2}{z_2 - z_1}\right) \tag{4}$$

The previous equations, Eqs. (3) and (4), can be considered still valid during ductile crack extension if the CTOD(δ) is measured at the initial crack tip position as shown in Fig. 6. Actually, several previous works have used the triangulation procedure, using two clip gages at different heights from the surface of specimen, to estimate *CTOD* values during fracture toughness tests in materials suffering stable ductile crack extension under increasing loads [31–33].

Additional information regarding the crack extension measurement by the compliance method for SE(B) and SE(T) specimens is presented now. Five elastic unloading cycles are performed at the beginning of the test (elastic response) to estimate and verify the initial crack size (a_0). Then, force controlled unloading cycles are performed at fixed CMOD intervals at the plastic regime. For the first five plastic unloading cycles the increase in CMOD before to make the unloading is equal to 0.02 mm and after that the intervals of 0.04 mm are used to perform the elastic unloading cycle. It should be noted that for the SE(T) specimens both the potential drop method and the elastic unloading compliance method provide excellent and comparable predictions of ductile crack growth according the experimental test performed by Verstraete [14,15].

3.2. Resistance curves for SE(B) and clamped SE(T) fracture specimens

Fig. 7 shows the obtained experimental resistance curves for both materials. The *CTOD* was measured by Eq. (3). The unloading elastic compliance method was used to measure the crack length evolution with the increase in remote loading. The elastic compliance equations were taken from CANMET procedure [34]. Crack length comparisons between the unloading elastic compliance method and direct current potential drop (DCPD) method have been performed using SE(T) specimens by [14]. It was concluded that both methods agree well with each other with a maximum differences less than 14%. The experimental tests were carried out under displacement control for both specimens, using a loading rate of 0.01 mm/s. In

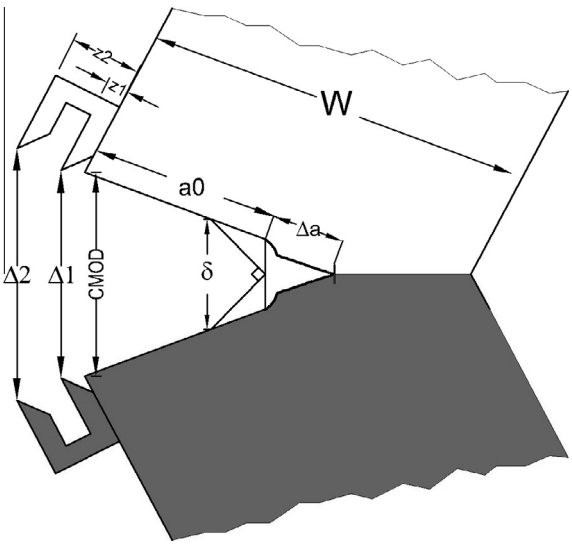

Fig. 6. CTOD measurement position during fracture toughness test.

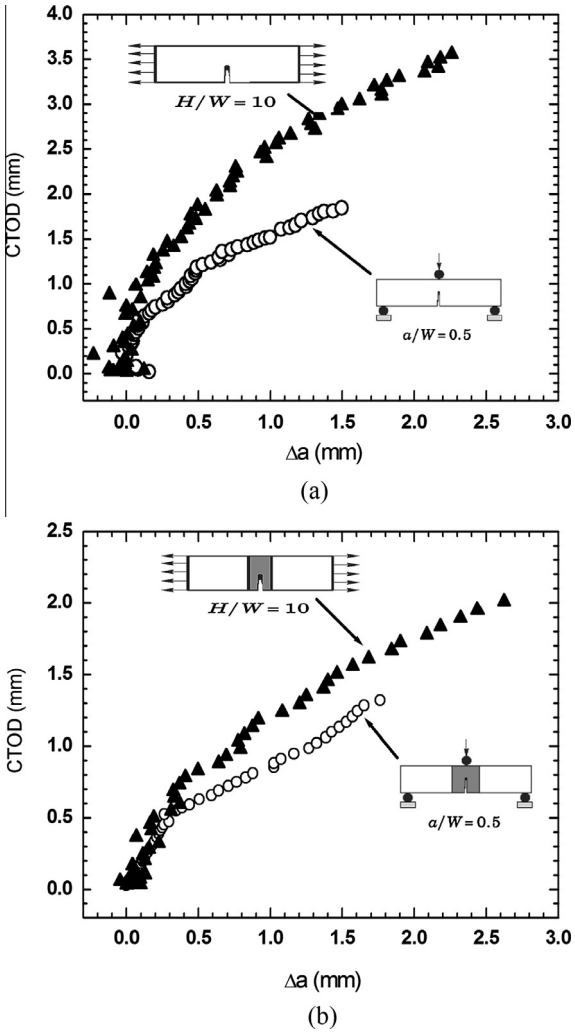

Fig. 7. CTOD-Δa curves obtained using SE(T) and SE(B) specimens: (a) samples extracted from base metal; (b) samples extracted from the girth welded pipe.

general terms, the fracture toughness rises in a nonlinear fashion with crack extension. As expected, the measured resistance curve is higher for the clamped SE(T) specimen than for the SE(B) specimen.

3.3. Resistance curves for Medium Wide Plates

Fig. 8 shows the measured *CTOD* versus Δa response for both materials during the wide plate testing. Two clip gages were attached to the specimen surface and from their readings the fracture toughness (*CTOD*) was calculated by Eq. (3). It is important to mention the necessary high loads $\left(\sim 1.5 \times 10^6 \text{ kN}\right)$ to test the large-scale specimens (MWP) when compared to small-scale specimens such as the SE(T) and SE(B) geometries where the maximum applied loads were in the order of 100 kN and 10 kN, see [14,15].

The ductile tearing was evaluated using the direct current potential drop (DCPD) method. The increase in potential drop (associated with an increased electrical resistance as the net cross section decreases upon crack growth) is measured close to the crack mouth. A second potential drop measurement (remote from the notch, in one of the base metals) provides a reference signal that is used to filter out undesired effects, such as external current leakage and material resistivity changes due to temperature variations. The transfer function between potential drop and crack growth is numerically derived from electrical finite element simulations. For further details about the DCPD procedure adopted for MWP specimens the reader is referred to [15].

The adopted potential drop procedure only provides the ductile crack extension after crack initiation has taken place. Therefore, the total amount of ductile tearing (Δa) consists of two components: crack growth due to crack blunting (Δa_B) and the crack extension measured by the direct current potential drop method (Δa_{CPD}). Initially, the former has been eval-

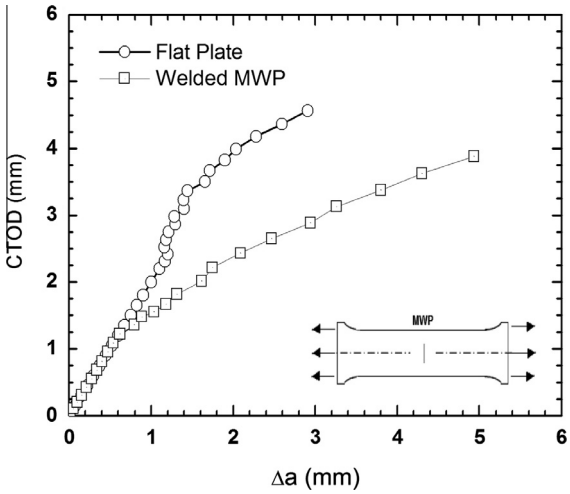

Fig. 8. Fracture toughness CTOD-Δa curves obtained using large-scale Medium Curved Wide Plate specimens extracted from the flat plate homogenous steel and the girth welded pipeline.

uated by Verstraete et al. [15] as the half of *CTOD* at the instant of initiation as suggested by Landes [35]. For this reason, it is possible to see a linear relation between *CTOD* and (Δa) at the beginning of the *R*-curve in Fig. 8.

The medium wide plate made of base metal API-5L X65 shows a steep rise after the initial portion of the CTOD-R curve. Also an apparent negative crack growth seems to be obtained during the experimental test. It is believed that the initial rising behavior ($1.0\ \text{mm} < \Delta a < 1.6\ \text{mm}$) of the curve is associated with the end of the blunting stage and initial crack growth. After the onset of stable crack growth, the curve seems to stabilize up to 3 mm of crack extension. This fracture response is commonly observed in ferritic steels and high strength low alloy steels. On the other hand, the apparent negative crack growth is related to uncertainties derived from the DCPD method such as spurious signals generated by electrical flow transmission, leakage current through holding fixtures. As a result, some scatter of crack growth is obtained directly from measurements. This experimental procedure resembles to the one in which the crack extension is correlated with the elastic compliance of the specimen. This method also produces negative values of growing crack.

4. Numerical procedures

Finite element analyses are described for 3-D models of bend and tension loaded crack configurations for side-grooved SE (B) and SE(T) fracture specimens and large-scale specimens (notched Medium Wide Plates). The analyses include material and geometric nonlinearities. The finite element models have nominal dimensions matching the real tested specimens. A detailed description of specimen dimensions is shown in Table 1. The next sections describe the finite element mesh necessary to model the ductile tearing phenomena by the computational cell approach and the constitutive material models used in the numerical simulations.

4.1. 3-D finite element models

The detailed crack growth analyses described in the present study explore the capability of the computational cell approach to describe constraint effects on ductile tearing for circumferentially cracked pipes, simulated by MWP, and typical fracture specimens as previously described. For these analyses, a fine mesh with computational cells ahead of crack front is used in 3-D settings. The arrangement of cell elements ahead of the Mode I growing crack follows closely the scheme depicted in Fig. 1(c). Fig. 9 shows the finite element models constructed for the 3-D analyses of the clamped SE(T) and SE (B) specimens.

To simulate ductile crack extension using the GT yielding model, a planar two-dimensional meshes are built for the SE(T) and SE(B) fracture specimens, containing a row of 75 computational cells along the remaining crack ligament $(W - a)$, as shown in Fig. 9. Then, the 3-D numerical models for these crack configurations are obtained by simply extruding the 2-D mesh along the transverse or *Z*-axis, see Fig. 9 for axis orientation. Only elements in the first row on the symmetry plane are defined with the GT yielding law. Symmetry conditions enable analyses using one-quarter of the specimen with appropriate constraints imposed on the symmetry planes. These numerical models have 20 variable thickness layers defined over the half-thickness $\left(\frac{B}{2}\right)$ with the thickest layer defined at mid-thickness $Z = 0.0$ as shown in Fig. 9. The first 15 layers are used to discretize the crack front and 5 layers describe the side groove area. The 15% side-grooves, 7.5% at each side, are introduced in each model by deleting the outermost 5 elements in the crack-plane. Then, the nodes in the groove area are trans-

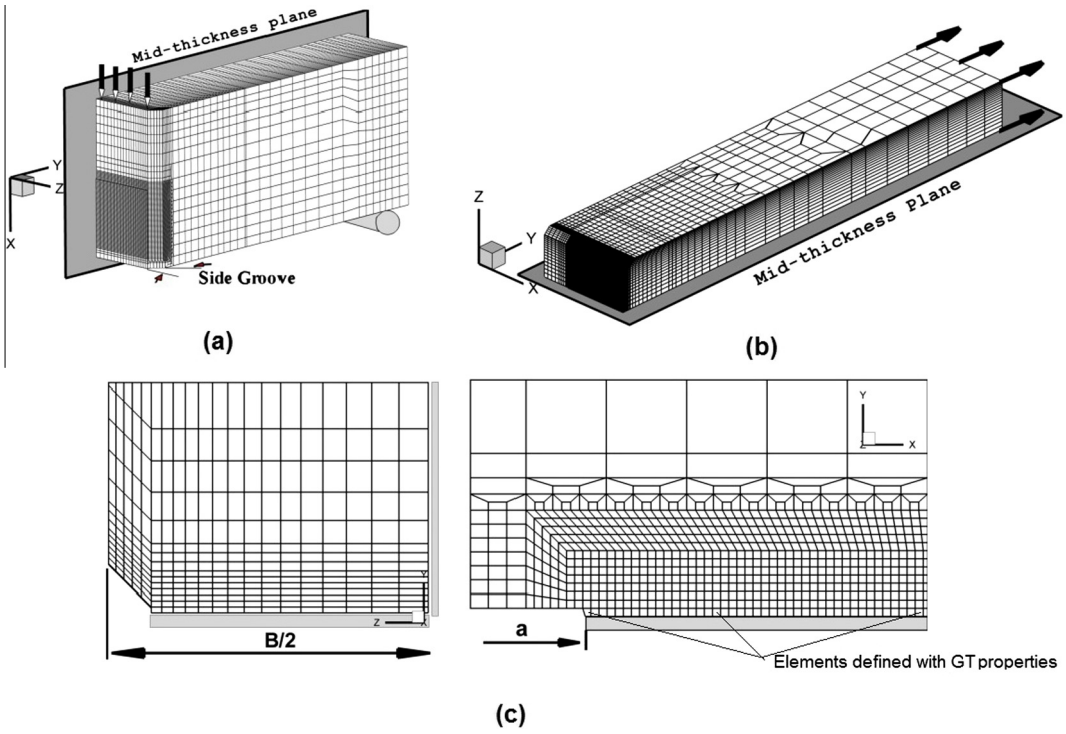

Fig. 9. Finite element mesh for fracture specimens with enlarged illustration of crack tip and side groove area: (a) SE(B); (b) SE(T); (c) zoom of crack tip mesh.

lated in the Y direction to match the specified side groove angle. As shown in Fig. 9(c), both specimens have identical mesh refinement at the crack tip damage zone and through the thickness.

The quarter-symmetric, 3-D models for these specimens have 34,400 nodes and 31,000 elements, approximately, with $75 \times 15 = 1125$ computational cells ahead of the crack front. The initially blunted crack tip accommodates the intense plastic deformation and initiation of stable crack growth in the early part of ductile tearing with blunt notch radius equal to $\frac{D}{2}$. The slab of 1125 computational cells over which damage occurs to model crack growth extends $0.5t$ ahead of the initial crack front.

Nonlinear 3-D finite element analyses including ductile tearing are also performed on cracked Medium Curved Wide Plate (MWP). Two MWP specimens are analyzed. The first MWP is extracted from a flat homogeneous plate and the second MWP is extracted from a girth welded pipe having dimensions matching the values provided in Table 1. The MWP specimens have a semi-elliptical surface flaw geometry.

Fig. 10 shows the finite element model for the welded Medium Curved Wide Plate specimen. The semi-elliptical flaw is located in the weld centerline at the inner surface emulating the experimental test. The crack front is described by 21 (circumferential) layers defined over the crack half-length (c); the mesh refinement through the crack half-length is such that smaller elements are created near the free surface and larger elements on the symmetry plane to accommodate the strong gradient in the stress distribution along the crack front. For each crack front layer, a row of 60 computational cells are arranged over the remaining crack ligament $(t - a)$ thereby enabling description of ductile crack extension along the crack front. Only elements localized on the symmetry plane are set with the GT yielding model. The quarter-symmetric models for these analyses have 26,000 8-node, 3-D elements (29,800 nodes) with appropriate constraints imposed on nodes defining the longitudinal symmetry plane and nodes on the remaining ligament. Like the previously SE(B) and SE(T) finite element models, these models are loaded by displacement increments imposed on the loading points providing a closer correspondence with the actual experimental conditions at the MWP specimen ends. Also, to accommodate large plastic strains at the onset of ductile tearing at the crack tip area, a blunt notch with a radius $\frac{D}{2}$ is introduced in the MWP specimen. The 3-D finite element model for the Medium Curved Wide Plate, related to the flat base homogeneous plate, has similar features to the MWP specimen previously described.

Modeling of welded specimens was performed in a simplified way. The weld fracture specimens are modeled as a bimaterial component with no transition region, i.e., the mechanical properties for the heat affected zone (HAZ) are not considered. Also, the modeled weld geometry has vertical groove face, bevel angle equal to zero and the weld cap height equal to zero; the weld groove width is set as $\frac{2h}{t} = 1$. Further, the reported misalignment of 1.6 mm (equal to 9% of the wall thickness) for the welded MWP specimen, see Fig. 3, has not been included in the finite element model. The previous simplifications

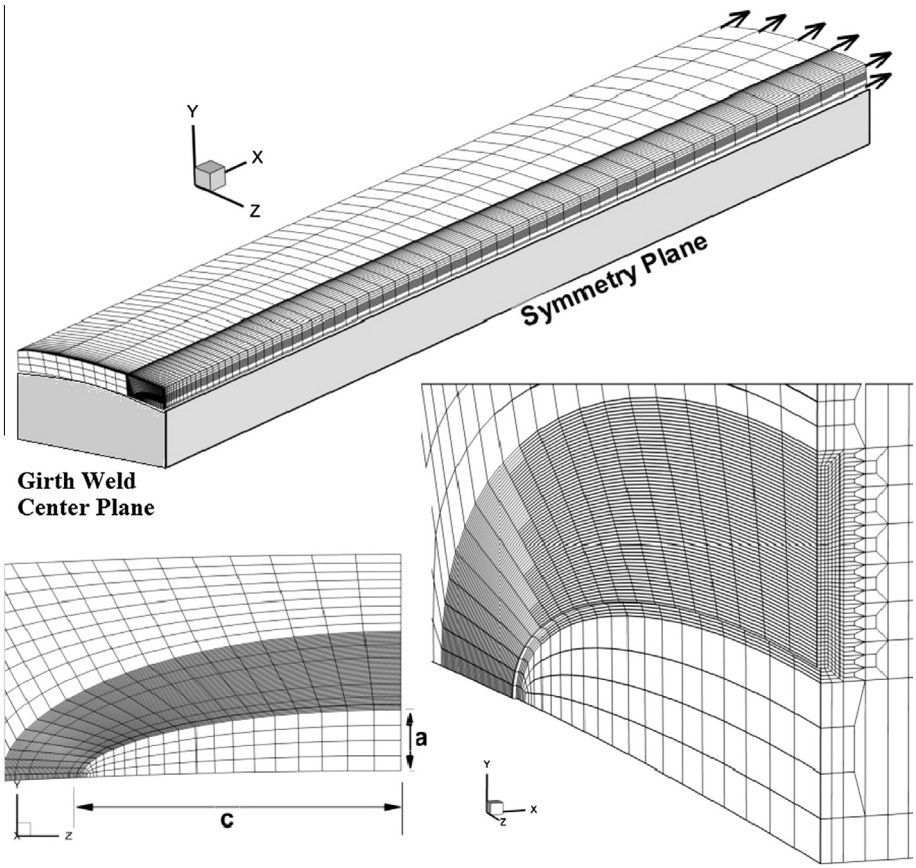

Fig. 10. Finite element mesh for Medium Curved Wide Plate having $a/t = 0.308, c/a = 4.78$, $L/W = 3.3$ and $D/t = 70.71$.

will have effects on the remote mechanical response. Probably, additional damage will be produced by the bending moment related to the misalignment of the weld and the stress concentration associated with the weld geometry (weld cap) itself. Therefore, the simplifications will have a strong influence on the remote strain/load response (i.e., on the tensile strain capacity of the MWP specimen), but not on the stress triaxiality near the crack tip (i.e., on the *R*-curve) which controls the void failure.

4.2. Material models and solution procedures

The mechanical characterization of different pipeline steels performed by Verstraete et al. [15] provides the necessary data to calibrate and validate the cell methodology to simulate ductile tearing in Medium Curved Wide Plate specimens. The program WARP3D [36] has the option to describe the inviscid uniaxial tensile stress-strain curve by a pure power-law after a linear response or using general piecewise-linear segmental description. In this study the uniaxial true stress vs. true strain behavior for the pipeline steels used is modeled with the piecewise linear option defined by the measured experimental tensile curve.

The elastic-plastic constitutive model for the material outside of the damage zone (see Fig. 1(a)) follows a common J_2 flow theory with conventional von Mises plasticity, undamaged by void growth, in large geometry change (LGC). The GT yielding law given by Eq. (1) is adopted to model the matrix material with initial voids and to describe the evolution of void growth and associated macroscopic material softening in the computational cells. The uniaxial true stress-logarithmic strain response for both the background and cell matrix materials follows the measured tensile response for the material at room temperature. The two adjustment factors q_1 and q_2 in the Gurson-Tvergaard yield condition given by Eq. (1) are given by Faleskog and Shih [23], who provide parameters q_1 and q_2 for a wide range of material flow properties (strain hardening properties, yield stress and Young' Modulus) for common pressure vessel and structural steels. For our study, this results in $q_1 = 1.517$ and $q_2 = 0.916$ for the base metal and $q_1 = 1.386$ and $q_2 = 0.972$ for the girth weld material. The q_3 parameter is defined by $q_3 = (q_1)^2$. Thus, the q_3 was set to 2.30 and 1.92 for the base metal and girth weld material, respectively.

The finite element code WARP3D [36] provides the numerical solutions for the 3-D crack growth simulations implementing the cell model. Evaluation of the *J*-Integral derives from a domain integral procedure which yields *J*-values in excellent

agreement with estimation schemes based upon η-factors for deformation plasticity in the fracture specimens [37] while, at the same time, retaining strong path independence for domains defined outside the highly strained material near the crack. In previous work [38] the path-independence of the $J-$Integral was checked during ductile crack growth using identical mesh refinement as shown in Fig. 9 for clamped SE(T) specimens having $\frac{a}{W}$ = 0.2 and 0.5. The material properties used in the verification of path-independence were those for an API X70 pipeline steel. The calculated $J-$Integral for both crack size ratios, $\frac{a}{W} = 0.2$ and $\frac{a}{W} = 0.5$, was weak path-dependence ($\sim 10\%$) with ductile crack extension, $\Delta a < 2$ mm. The size of the largest integration domain for the path-independence verification was equal to 15D. WARP3D analyzes fracture models constructed with three-dimensional, 8-node trilinear hexahedral elements. WARP3D options include a fully automatic crack growth procedure by element extinction. After the element attains a critical void fraction (f_E), its stiffness is set to zero and the nodal forces exerted by the element on adjacent nodes are relaxed to zero over a simpler linear-traction separation model. In this procedure the element is not topologically deleted from the model but it no longer contributes any resistance to loading [36]. Also, WARP3D provides an adaptive load control feature that automatically decreases or increases subsequent load step sizes based on the rate of porosity increase in the model. This adaptive load control is done to improve Newton convergence of the global load that can be adversely affected by the element extinction procedure. Gullerud et al. [20] have shown that the adaptive load control does not have an effect on predicted resistance curve.

4.3. Outline of the calibration process of cell parameters f_0 and D

In order to apply the cell approach for modeling ductile crack extension five parameters have to be defined: f_0, D, q_1, q_2 and f_E . As previously described, q_1 and q_2 are related to the hardening response of the matrix material and they are determined using the proposal of Faleskog and Shih [23]. Previous experience with crack growth simulations [6,39] has shown that numerical predictions are not sensitive to f_E value when its value is between 0.15 and 0.2. In the current study, f_E was set to 0.15.

After q_1, q_2, and f_E are determined, numerical simulation of ductile tearing in the fracture specimens described here begins with calibration of the cell parameters f_0 and D. The cell size D and initial porosity f_0 define the key parameters coupling the physical and computational models for ductile tearing. Although the parameters f_0 and D are micro-structurally based, it is difficult to apply values determined by metallurgical observations directly into the GT yielding model due to the intrinsic idealizations in the model [40]. Xia et al. [41] observed that D and f_0 do not necessarily represent actual physical-metallurgical properties (mean void sizes and initial void volume fraction) and should be considered as computational phenomenological parameters calibrated by matching numerical results to experimental test data. In this study, the initial void volume fraction and cell size were determined by fitting experimental results obtained from SE(B) specimens taken from the homogeneous flat plate and SE(T) specimens taken from the girth weld pipe. Once f_0 and D parameters have been determined, they can be assumed to be *material properties* applicable to the analysis of structural integrity for structural components under different types of loading conditions (such as traction and bending loads).

Since every change in D requires the construction of a new finite element mesh, the effort of calibration will be obviously reduced if D is fixed and, next, the value of f_0 is estimated by a series of finite element analyses which try to match numerical R-curve to experimental $J(\delta) - \Delta a$ data. In order to capture the active micro-mechanism of fracture process coupled to the high gradient of stresses ahead of the crack under propagation, the calibration process should preferably use precracked fracture specimens. Although *high constraint* SE(B) or C(T) geometries with deep cracks ($\frac{a}{W} \geqslant 0.5$) are commonly employed for calibration of f_0 in structural steels [6,18,22,42–45], novel recent publications have shown that it is possible to calibrate f_0 and D parameters using geometries with low levels of plastic constraint [9,12,40,46,47]. Therefore, two procedures to calibrate the parameters f_0 and D were considered during this study:

1. Starting from experimental results of SE(B) specimens with deep cracks ($\frac{a}{W} = 0.5$), a 3-D finite element model was constructed with identical dimensions to the experimental test and the pairs of parameters $f_0 - D$ were determined by reproducing the experimental data. During the matching of experimental and numerical R-curves D is fixed and f_0 is changed. After calibration of cell parameters, numerical predictions of $\delta - \Delta a$ curves in SE(T) specimen with $\frac{a}{W} = 0.2$ and MWP specimen having $\frac{a}{t} = 0.2$ were made and directly compared with the experimental measurements carried out by Verstraete et al. [15]. This procedure was applied in the tests conducted on the base homogeneous metal steel. As shown in Section 3, this material corresponds to a steel grade API-5L X65.
2. Using the experimental data of SE(T) specimens with crack size ratio $a/W = 0.3$, 3-D finite element models, with dimensions matching tested specimens, were used to bring the numerical and experimental CTOD-R curves into close agreement by changing f_0 while D is fixed. Finally, numerical predictions of $\delta - \Delta a$ curves in SE(B) with $\frac{a}{W} = 0.5$ and MWP with $\frac{a}{W} = 0.3$ were made and directly compared with the experimental data. In this case, the computational analyses were carried out on specimens extracted from girth welds of a pipeline with $D' = 1219$ mm and thickness $t = 17$ mm. The base metal is a high grade pipeline steel API-5L X80.

The main reason for performing different calibration procedures is to check the robustness of the computational cell methodology to predict toughness resistance curves for geometries with different levels of stress triaxiality. Previous studies

[9,46,47] have reported good performance of Gurson-Tvergaard yielding model in predicting *R*-curves for circumferentially cracked pipes using low constraint specimen, SE(T), to calibrate the computational cell model.

Experience with past finite element analyses of fracture specimens to estimate the cell size for common pipelines and pressure vessel steels suggests values of 50–200 mm for D [6,18–20,24,38,42,43,48,49]. For this reason, in this study the cell size is adopted as $D = 200$ μm for all numerical models. This size provides an approximate correlation of spacing between the large inclusions and the crack tip opening displacement (*CTOD*) at the onset of macroscopic crack growth in conventional fracture specimens for common pressure vessel steels while, at the same time, providing adequate resolution of the stress-strain fields in the active layer and in the adjacent background material. These numerical models are loaded by displacement increments imposed on the loading points, see Fig. 9, which permits continuation of the analyses after the load starts decreasing due to crack growth.

5. Numerical evaluation of crack growth resistance curves

This section reports numerical predictions of geometric effects on resistance curves obtained by the computational cell methodology described before. In order to begin the comparisons between experimental and numerical *CTOD-R* curves, it is necessary to obtain the material properties that govern the fracture behavior of computational cells. Thus, one essential task to start simulations using the previously described micro-mechanics methodology is the calibration of f_0 (initial void fraction). As already noted, this parameter governs the response of the computational cell model and needs to be calibrated using experimental toughness data.

5.1. Comparison between experimental and numerical resistance curves for the base metal API-5L X65 steel

For this material, the parameters governing the response of computational cells, $f_0 - D$, were calibrated by matching numerical and experimental *R*-curves for SE(B) specimens having high crack size ratio $\left(\frac{a}{W} = 0.5\right)$. Importantly, these calibrated parameters were used to predict the response for SE(T) and MWP specimens having shallow cracks $\left(\frac{a}{W} = \frac{a}{t} = 0.2\right)$.

Fig. 11 compares the experimental and predicted *R*-curves for a deeply cracked SE(B) specimen. Experimental results were obtained from two nominally identical specimens (i.e. identical geometries within an acceptable dimensional tolerance range); the experimental data are indicated by symbols as shown in Fig. 11. Both specimens show an apparent negative crack growth. This is a well-known problem during fracture testing of SE(B) and SE(T) specimens. Similar experimental behavior can be found in previous articles [7,33]. Different explanations have been given: friction, misalignment, specimen rotation, residual stresses during unloading, analysis method, localized deformation, etc. The precise causes of this phenomenon are not fully understood and further studies are needed.

Predicted *R*-curves are shown for two values of the initial volume fraction $(f_0 = 0.0001, 0.000135)$. As can be seen in Fig. 11(a), for $f_0 = 0.0001$ there is a good agreement between experimental data and the predicted numerical resistance curve. On the other hand, $f_0 = 0.000135$ yields a lower resistance curve. The numerical predictions deviate from experimental results for $\Delta a[mm] \leq 0.3$ in the blunting region. Xia and Shih [50] have already discussed the poor behavior of cell approach to capture the blunting effects. Although numerical simulation fails to predict the exact moment of deviations from the "blunting line", the agreement is improved for crack growth higher than $\Delta a \geqslant 0.5$ mm.

After key parameters f_0 and D have been obtained, the following studies focus on numerical predictions of resistance curves for clamped SE(T) and Medium Curved Wide Plate. All numerical measurements $(\Delta a, \delta)$ correspond to the midplane

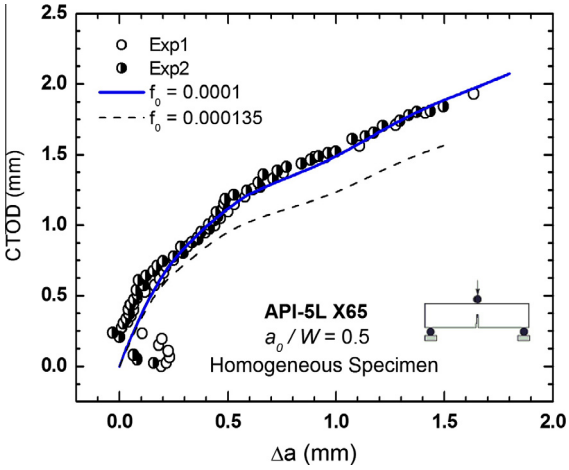

Fig. 11. Calibration of cell parameters f_0 using high constraint specimen.

location corresponding to $\frac{Z}{(B/2)} = 0$, see Fig. 9(b). For the case of MWP specimens with elliptical crack front, the numerical results are evaluated at the deepest point of the elliptical surface crack.

First, we consider the SE(T) geometry with dimensions shown in Table 1. The numeric resistance *R*-curve is estimated using the previous calibrated value of initial porosity ($f_0 = 0.0001$), see Fig. 12. In general terms, the predictions of the $CTOD - \Delta a$ values using the computational cell model correlate well with the experimental measurements until $\Delta a \approx 2$ mm, having differences on *CTOD* values less than 15% for an equal value of Δa.

Fig. 12 reveals an interesting result. The *CTOD* measured at the original crack tip using the 90° definition matchs the *CTOD* calculated by Eq. (3). The CTOD 90° was obtained by the interception of two −45° lines starting at original crack tip with the deformed crack flank profiles, see [39,51] for illustration of this definition. The agreement between both definitions is better for $\Delta a \leqslant 2.0$ mm. It must be commented that the experimental results shown in Fig. 12 correspond to two SE(T) specimens. It also has to be noted the good repeatability of the experimental results coming from two different specimens.

We now direct attention to the MWP geometry, shown in Fig. 2(a), and its 3-D mesh model in Fig. 10. The predicted *R*-curve curve comes from numerical analysis of computational model with shallow crack ($\frac{a}{t} = 0.2$) and using the previous calibrated value $f_0 = 0.0001$. Although the numerical simulation produces a higher initial tearing slope (blunting line) than the experimental results and consequently greater resistance curve, the agreement is improved when the original experimental data provided by [14] are modified as explained in the next paragraph.

One additional explanation has to be made related to comparisons shown in Fig. 13. Before the crack begins to tear, the intense local plastic deformation at the crack tip causes an increase in the *CTOD*. This plastic blunting effect causes the tip of the crack to move forward. The potential drop method only provides crack growth values without considering the increase in crack length associated with the blunting of the crack tip. Verstraete et al. [15] added one empirical correction to potential drop measurement using a proposal made by Landes [35]. The increment on crack length, associated to crack tip blunting, may be obtained as follows:

$$\Delta a_{Blunting} = \delta_{Ic}/M \tag{5}$$

where δ_{Ic} is the *CTOD* for initiation of stable crack growth and $M = 2$. Broek [52] showed some experimental evidences that the *CTOD* at crack initiation by dimple rupture is twice the stretched zone for Al-Zn-Mg alloy forgings. However, further research has shown that *M* is actually dependent on strain hardening exponent [53,54]. Mills [53] obtained experimental fracture data with a well-defined blunting line by using $M \sim 3$ in Eq. (5). Thus, *M* could take values between $2 \leqslant M \leqslant 3$ [53,54]. As a consequence of these results, better agreement between predicted and experimental resistance curves for MWP specimens was obtained by setting $M = 3$ in Eq. (5) to define the initial blunting line. The experimental data evaluated with both values of *M* are shown in Fig. 13. As shown in Fig. 13, there is a satisfactory agreement between experimental and numerical curves until $\Delta a \approx 2.0$ mm. Considering the previous results, it can be said that the computational cell model is able to make acceptable predictions of the real mechanical response, in terms of *R*-curve, of MWP specimen with shallow crack.

To close this section it would be interesting to note the ability of the GT yielding model to predict *R*-curves for specimens with different levels of stress triaxiality such as the clamped SE(T), Medium Wide Plate (MWP) and SE(B) geometries.

5.2. Comparison between experimental and numerical resistance curves for the welded joint

Given the good performance of the computational cell-based model in the previous Section 5.1 for geometries with different levels of plastic constrain and loading modes, it was decided to calibrate the parameters (f_0, D), governing the

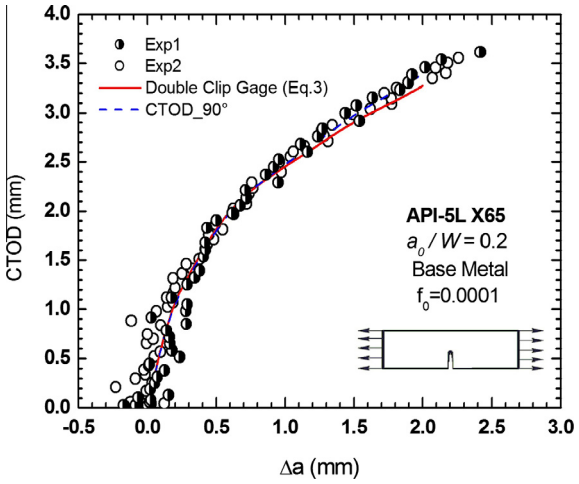

Fig. 12. Comparison between predicted and numerical *R*-curves for homogeneous clamped SE(T) specimen.

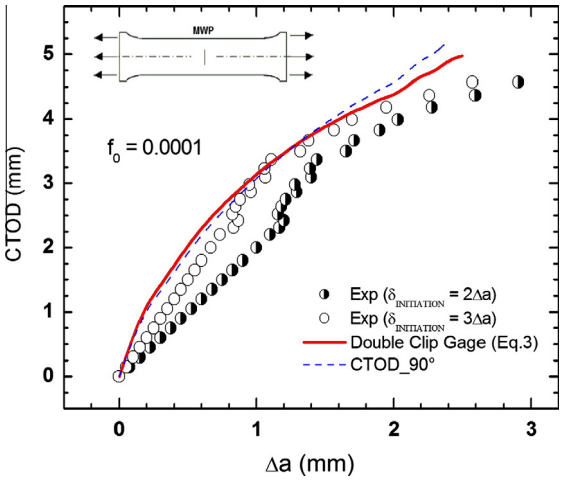

Fig. 13. Comparison of experimental measured and numerical predicted *R*-curve for Medium Curved Wide Plate made of base metal grade API 5L X65 steel.

response of the computational cells by matching experimental resistance curves from clamped SE(T) specimens with initial notch $\frac{a}{W} = 0.3$, as has been explained before in Section 4.3.

Next, the calibrated parameters were used in numerical analysis of the pre-cracked SE(B) configuration with initial crack ratio $\frac{a}{W} = 0.5$ and MWP specimen with an elliptical notch having $\frac{a}{t} = 0.3$ and $\frac{2c}{a} = 9.5$.

Fig. 14 compares experimental and numerical *R*-curves for the SE(T) specimen tested by [15]. Experimental results correspond to two nominally identical samples; experimental data are indicated by symbols as shown in Fig. 14. The numerical predictions considering two values for f_0 are shown in Fig. 14. It is observed that the simulation with $f_0 = 0.0005$ matches in a successful way the experimental data. In contrast, the *R*-curve obtained with $f_0 = 0.0002$ is much higher than the experimental *CTOD* curve for the same amount of Δa. Therefore, the tuned parameters $f_0 = 0.0005$ and $D = 200$ μm can be regarded as properties of the girth weld joint.

Let us make some comments about the parameter f_0 for both materials used in this study. It is not expect any similarity or correlation between the calibrated initial void sizes for both materials. It can be said that the small initial void size for the base metal looks reasonable because the homogeneous base plate is expected to have less metallurgical imperfections (such as inclusions or oxides) than the welded joint. In addition, the higher *R*-curve for the base metal is responsible for the lower initial void size when compared to the weld metal due to both numerical models used the same cell size *D*.

After key parameters f_0 and *D* have been calibrated, the following studies focus on numerical predictions of resistance curves for deeply notched SE(B) specimen and shallow notched Medium Curved Wide Plate (MWP). Noteworthy is the good repeatability of the experimental results coming from two different SE(T) specimens.

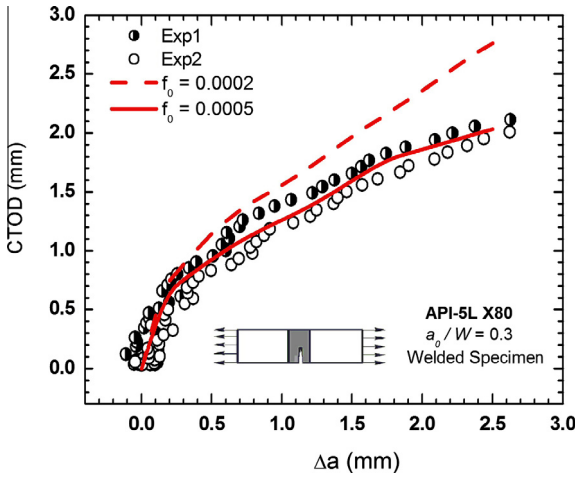

Fig. 14. Calibration of f_0 and *D* parameters for API X80 steel and its welded joint using low constraint SE(T) specimen.

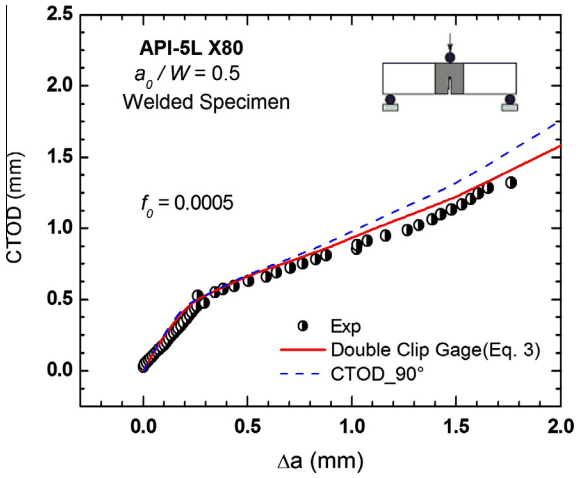

Fig. 15. Comparisons between predicted and measured *R*-curves curves for deeply notched SE(B) welded specimen.

First, the SE(B) specimen was considered having the dimensions detailed in Table 1. Fig. 15 displays the simulated $\delta - \Delta a$ curve along with the experimental results. The predicted *R*-curve through the computational cell model shows excellent correlation with the experimental measurements up to $\Delta a \approx 1.8$ mm, showing minimal differences in δ for a given Δa value. Estimation of *CTOD* (δ) and Δa for SE(B) samples was made using Eq. (3) and the direct potential drop method, respectively. The crack growth during the blunting phase was defined by using $M = 2$ in Eq. (5). Further, note the good agreement between both definitions of *CTOD*, by using Eq. (3) and the 90° intercept definition at the original crack tip, for small crack extension($\Delta a \leq 1.5$ mm).

We consider now the MWP geometry as shown in Fig. 2(a) and its finite element mesh shown in Fig. 10. The numerical predictions are performed through numerical analysis for the computational cell model using the value $f_0 = 0.0005$. Fig. 16 shows the numerical $\delta - \Delta a$ curve along with the experimental results. As seen in Fig. 16, the micro-mechanics cell approach is able to predict the toughness variation with increasing crack growth for the Medium Curved Wide Plate. The computational cell model emulates virtually the whole resistance curve for shallow welded notched MWP specimen, particularly on the range $\Delta a \leq 2.0$ mm. It should be noted that we have plotted for comparison reasons the experimental data using two values of parameter *M* to define the blunting line. As can be seen in Fig. 16 a better agreement is obtained between experimental and numerical *R*-curves when the crack extension due to the blunting of the crack is defined by Eq. (5) with $M = 3$.

Let us include some comments regarding the adopted cell size and its correlation with spacing between inclusion and CTOD. As indicated in the manuscript *D* and f_0 parameters do not necessarily represent the actual physical-metallurgical properties, and both parameters should be viewed as computational parameters that bring into agreement the experimental

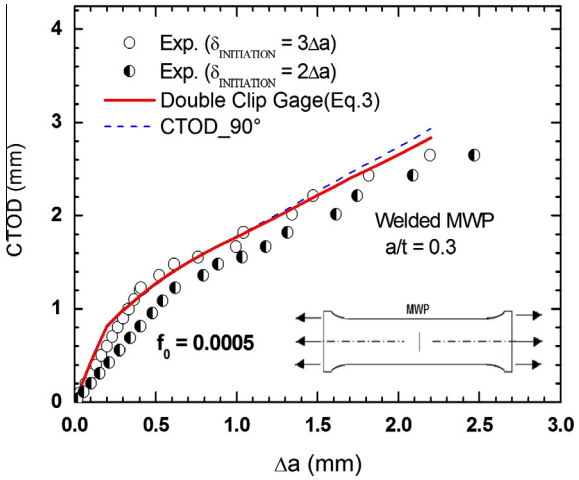

Fig. 16. Comparisons between predicted and measured *R*-curves for MWP welded specimen.

and measured *R*-curves. We did not perform metallurgical characterization of both materials so it is not possible to confirm the hypothesis that *D* is correlated with the spacing of large inclusions.

At the time when the GT yielding model was proposed limited computational resources and experimental data were available. Thus, at the original Shih et al's proposal in 1995 [18], they argued that an initial chose of parameter *D* should be in the order of the CTOD at the moment of fracture initiation ($CTOD_{Ic}$). They stated that the $CTOD_{Ic}$ is typically equal to several times the mean void spacing. In this study the CTOD at the onset of stable crack growth for the small specimens was around 0.5 mm and for the large-scale specimens (MWP) was around 1.5 mm. Thus, the adopted cell size, $D = 0.2$ mm, is 40% of the $CTOD_{Ic}$ for the small-scale specimens and roughly 14% for the large-scale MWP. Therefore, the chosen cell size for these specific materials can be tough to be related to the $CTOD_{Ic}$ only for the small specimens. Nevertheless, the cell methodology with the chosen cell size and calibrated initial void size were able to reproduce the *R*-curves for both tested materials.

To summarize, previous results shown in Figs. 11–16 demonstrate the good *transferability* of *R*-curves between different geometries having low and high stress triaxiality. It has to be noted that 3-D numerical analyses provide consistent results when compared to experimental ones. Parameter f_0 was calibrated using high and low constraint specimens and then numerical predictions for different geometries were carried out by finite element computations. These numerical results were compared with experimental tests. Generally speaking, the comparisons produced good matches for homogeneous and welded specimens. Consequently, it was shown that the initial porosity parameter f_0 used in the Gurson-Tvergaard yielding model is essentially a *material constant* when the ductile failure mode is governed by the mechanism of growth and coalescence of voids.

6. Concluding remarks

The main purpose of Wide Plate Test was to simulate as closely as possible the tensile load bearing and strain capacity of steel plates and their welded configurations. The usual information obtained from a wide plate test is the resistance to initiate and propagate a crack and its strain capacity. The extensive set of nonlinear finite element analyses for 3-D models of clamped SE(T) and 3P SE(B) specimens has shown the feasibility of modeling the ductile behavior of notched curved wide plates by a micro-mechanics approach, based upon the computational cell methodology incorporating the Gurson-Tvergaard yielding law. The current results support the following conclusions:

- Predictions of fracture resistance curve obtained in this work are acceptable. The agreement is equal for homogeneous and welded specimens. Predicted *R*-curves for the Medium Curved Wide Plate specimens agree relatively well with experimental data when the crack extension due to blunting is defined as three times the CTOD at the onset of ductile crack propagation in the measured fracture toughness data.
- The model to correlate the CTOD at initiation with the crack extension due to the blunting of the crack deserves further investigation. In this study it was necessary to modify the Joyce's proposal to get better correlations between the numerical and experimental results for the Medium Wide Plate specimens.
- Similar predictions of *CTOD* have been obtained using the double clip gage triangulation and the 90° intercept definition.
- The cell approach provides good predictions of the mechanical response of medium curved wide plates when the model parameter are calibrated by either the high constraint SE(B) specimen or the low constraint clamped SE(T) specimen.
- The cell model is a reliable tool to make predictions about the fracture behavior (including ductile crack growth) of large-scale structures using small fracture specimens to calibrate the internal damage parameters (f_0, D). However, it is worth emphasizing that predictions were acceptable because only a flat fracture surface was developed during the ductile tearing, i.e. there is no important contribution to the fracture behavior from others modes such as slant failure. More advanced failure criteria and material constitutive laws are necessary to simulate fracture problems where such behavior has an important role. During the last few years there exists an intensive effort to improve the capability of failure models by taking into account the influence of the third invariant of the deviatoric stress tensor on the failure criterion and yielding law [55,56].

Overall, the results obtained in this work revealed the computational cell-based approach as a valid engineering tool to predict ductile crack growth behavior in flawed structural component. Advanced methodologies for fracture assessment of pipelines must include robust procedures to *transfer* fracture resistance data measured using small laboratory specimens to real full-scale pipes in engineering applications.

Acknowledgments

This investigation is supported by Fundação de Amparo á Pesquisa do Estado de São Paulo (FAPESP) through a graduate scholarship (2012/0094-2 and 2013/01139-2) provided to the first author (DFBS). The co-authors from Ghent University would like to acknowledge the financial support of the IWT (Agency for Innovation by Science and Technology – Grant Nos. SB-091512 and SB-093512) and the FWO (Research Foundation Flanders – Grant Nos. 1.1.880.09.N.00 and 1.1.880.11.N.01). The work of CR is supported by the Brazilian Council for Scientific and Technological Development (CNPq) through Grants 306193/2013-2 and 456222/2013-8.

References

[1] Hutchinson JW. Fundamentals of the phenomenological theory of nonlinear fracture mechanics. J Appl Mech 1983;50:1042–51.
[2] Anderson TL. Fracture mechanics: fundamentals and applications. 3rd ed. Boca Raton (FL): CRC Press; 2005.
[3] Det Norske Veritas. Fracture control for pipeline installation methods introducing cyclic plastic strain. DNV-RP-F108; 2006.
[4] British Institution. Method of test for determination of fracture toughness in metallic materials using single edge notched tension (SENT) specimens. BS 8571; 2014.
[5] Nyhus B, Østby E, Knagenhjelm H, Black S, Røstasand P. Experimental studies on the effect of crack depth and asymmetric geometries on the ductile tearing resistance. In: ASME, editor. 24th International conference on ocean, offshore and arctic engineering (OMAE), Halkidiki, Greece.
[6] Sarzosa DFB, Ruggieri C. A numerical investigation of constraint effects in circumferentially cracked pipes and fracture specimens including ductile tearing. Int J Press Ves Pip 2014;120–121:1–18.
[7] Park DY, Tyson WR, Gianetto JA, Shen G, Eagleson RS. Evaluation of fracture toughness of X100 pipe steel using SE(B) and clamped SE(T) single specimens. In: International pipeline conference (IPC).
[8] Fairchild D, Cheng W, Ford S, Minnaar K, Biery ANE, Nissley Kumar N, et al. Recent advances in curved wide plate testing and implications for strain-based design. In: 17th International offshore and polar engineering conference (ISOPE), Lisbon, Portugal.
[9] Liu M, Wang Y-Y. Applying Gurson type of damage models to low constraint tests of high strength steels and welds. In: ASME, editor. 6th International pipeline conference (IPC), Calgary, Canada.
[10] Richards M, Weeks T, McColskey D, Wang B, Wang Y-Y. Fatigue pre-cracking curve wide plates in bending. In: ASME, editor. 8 th International pipeline conference, Calgary, Canada.
[11] Verstraete M, Hertelé S, De Waele W, Denys R, Van Minnebruggen K. Constraint analysis or curved wide plate specimens. In: ESIS, editor. 19th European conference on fracture, Kazan, Russia.
[12] Chen Y, Lambert S. Numerical modeling of ductile tearing for semi-elliptical surface cracks in wide plates. Int J Press Ves Pip 2005;82:417–26.
[13] Hertelé S, de Waele W, Denys R, Verstraete M. Investigation of strain measurements in (curved) wide plates specimens using digital image correlation and finite element analysis. J Strain Anal 2012;47(5):276–88.
[14] Verstraete M. Experimental-numerical evaluation of ductile tearing resistance and tensile strain capacity of biaxially loaded pipelines Ph.D. thesis, 2013.
[15] Verstraete M, De Waele W, Minnebruggen KVan, Hertelé S. Comparison of girth weld tearing resistance obtained from curved wide plate and single edge notch tensile testing. Eng Fract Mech 2015;148:406–20.
[16] Gurson A. Continuum theory of ductile rupture by void nucleation and growth: Part I-Yield criteria and flow rules for porous ductile media. J Eng Mater Technol 1977;99:2–15.
[17] Tvergaard V. Material failure by void growth to coalescence. Adv Appl Mech 1990;27:83–151.
[18] Xia L, Shih CF. Ductile crack growth-I. A numerical study using computational cells with microstructural-based length scales. J Mech Phys Solids 1995;43:233–59.
[19] Xia L, Shih C. Ductile crack growth-II. Void nucleation and geometry effects on macroscopic fracture behavior. J Mech Phys Solids 1995;43:1953–81.
[20] Gullerud A, Gao X, Dodds R, Haj-Ali R. Simulation of ductile crack growth using computational cells: numerical aspects. Eng Fract Mech 2000;66:65–92.
[21] Garrison Jr WM, Moody NR. Ductile fracture. J Phys Chem Solids 1987;48:1035–74.
[22] Ruggieri C, Dodds RH. Numerical modeling of ductile crack growth using computational cell elements. Int J Fract 1996;82:67–95.
[23] Faleskog J, Shih C. Cell model for nonlinear fracture analysis – I: Micromechanics calibration. Int J Fract 1998;89:355–73.
[24] Ruggieri C, Dodds RH. A transferability model for brittle fracture including constraint and ductile tearing effects: a probabilistic approach. Int J Fract 1996;79:309–40.
[25] Besson J. Continuum models of ductile fracture: a review. Int J Damage Mech 2010;19:3–52.
[26] Andrews R, Denys R, Knauf G, Zarea M. EPRG guidelines on the assessment of defects in transmission pipeline girth weld – revision 2014. J Pipeline Eng 2015;14:9–21.
[27] Akourri O, Louah M, Kifani A, Gilgert G, Pluvinage G. The effect of notch radius on fracture toughness J. Eng Fract Mech 2000;65:491–505.
[28] ExxonMobil. Measurement of crack tip opening displacement CTOD and J-fracture resistance curves using single-edge notched tension (SENT) specimens. Tech rep. ExxonMobil Upstream Research Company; 2010.
[29] American Society for Testing and Materials. Standard test method for measurement of fracture toughness. ASTM E1820-2011; 2011.
[30] German Institute for Normalization. DIN EN 10002: testing of metallic materials-tensile test pieces; 2009.
[31] Moore LP, Pisarski H. Validation methods to determine CTOD from SENT specimens. In: 22nd International ocean and polar engineering conference. Rhodes (Greece): ISOPE; 2012.
[32] Pussegoda L, Tyson WR, Gianetto J, Shen G, Pisarski H. Comparison of resistance curves from multi-specimen and single-specimen SEN(T) tests. In: 23rd International offshore and polar engineering. Alaska (USA): ISOPE; 2013.
[33] Park D, Gravel J, Simha C, Liang J, Duan D. Low-constraint toughness testing of two SE(T) methods in a single specimen. In: ASME, editor. Pressure Vessels and Piping Conference (PVP), PVP2014, Anaheim, CA, USA.
[34] Recommended practice: fracture toughness testing using se(t) samples with fixed-grip loading. Tech rep. CANMET; 2010.
[35] Landes J. The blunting line in elastic-plastic fracture mechanics. Fatigue Fract Eng Mater Struct 1995;18:1289–97.
[36] Gullerud A, Koppenhoefer K, Roy A, RoyChowdhury S, Walters M, Dodds RJ. Warp3D-release 15.9: 3-D dynamic nonlinear fracture analysis of solids using parallel computers and workstations.
[37] Moran B, Shih CF. A general treatment of crack tip contour integrals. Int J Fract 1987;35:295–310.
[38] Sarzosa DFB, Souza R, Ruggieri C. J-CTOD relations in clamp SE(T) fracture specimens including 3-D stationary and growth analysis. Eng Fract Mech 2015;147:331–54.
[39] Sarzosa DFB, Ruggieri C. Relations between J and CTOD in SE(T) and SE(B) specimens for stationary and growing cracks. In: 10th International pipeline conference, Calgary, Canada.
[40] Chen Y, Lambert S. Analysis of ductile tearing of pipeline-steel in single edge notch tension specimens. Int J Fract 2003;124:179–99.
[41] Xia L, Shih F, Hutchinson JW. A computational approach to ductile crack growth under large scale yielding conditions. J Mech Phys Solids 1995;43 (3):389–412.
[42] Ruggieri C, Dotta F. Numerical modeling of ductile crack extension in high pressure pipelines with longitudinal flaws. Eng Struct 2011;33:1423–38.
[43] Hippert E, Ruggieri C. Experimental and numerical investigation of ductile crack extension in a high strength pipeline steel. In: ASME, editor. 2001 Pressure vessels & piping conference (PVP 2001), Atlanta, GA,USA.
[44] Gao X, Faleskog J, Shih C, Dodds R. Ductile tearing in part-through cracks: experiments and cell-model predictions. Eng Fract Mech 1998;59(6):761–77.
[45] Benseddiq N, Imad A. A ductile fracture analysis using local damage model. Int J Press Ves Pip 2008;85:219–27.
[46] Dybwad J, Törnqvist R, Ostby E, Thaulow C. Simulations of ductile tearing at large strains of biaxially loaded pipes. In: ASME, editor. 28th International conference on ocean, offshore and arctic engineering (OMAE), Honolulu, Hawaii, USA.
[47] Huang T, Fairchild DP, Panico M, Crapps J, Cheng W. Strain capacity prediction of strain-based pipelines. In: ASME, editor. 10th International pipeline conference (IPC), Calgary, Canada.
[48] Xia L, Shih CF. Ductile crack growth – III: Transition to cleavage fracture incorporating statistics. J Mech Phys Solids 1996;44:603–39.
[49] Ruggieri C, Dodds RH. Probabilistic modeling of brittle fracture including 3-D effects on constraint loss and ductile tearing. J Phys 1996;6:353–62.

[50] Xia L, Shih CF. Ductile crack growth – I: A numerical study using computational cells with microstructurally-based length scales. J Mech Phys Solids 1995;43:223–59.
[51] Sarzosa DFB, Ruggieri C. Experimental validation of relationship between fracture parameters J and CTOD for SE(B) and SE(T) specimens during ductile crack growth. Mar Syst Ocean Technol 2015;10(1):60–70.
[52] Broek D. Correlation between streched zone size and fracture toughness. Eng Fract Mech 1974;6:173–81.
[53] Mills WJ. On the relationship between stretch zone formation and the J-integral for high strain hardening materials. J Test Eval 1981;9(1):56–62.
[54] O'Brien D, Fergurson W. On the J-Integral blunting line for soft materials. Int J Fract 1982;20:R39–43.
[55] Nahshon K, Hutchinson JW. Modification of the Gurson model for shear failure. Eur J Mech – A/Solids 2008;27:1–17.
[56] Ohata M. Damage model for simulating large ductile crack extension accompanied by flat and slant surface. In: Technical T, editor. International pipeline conference.